

# Research Article



**Batteries** 

How to cite: Angew. Chem. Int. Ed. 2025, e13842 doi.org/10.1002/anie.202513842

# **Electroactive Chelating Groups Enable High-Performance Aqueous Zinc-Organic Batteries**

Jin Zhou $^+$ , Hongbin Xu $^+$ , Peifang Guo, Jihuang Jiao, Yufei He, Qiangqiang Wang, Xingyu Ding, Da Liu, Ju Li,\* and Renbing Wu\*

**Abstract:** P-type organic electrode materials, characterized by fast kinetics and high redox potential, hold great promise for aqueous zinc-ion batteries (ZIBs), but suffer from low capacity and limited cycling stability in practical applications. Herein, we demonstrate that the introduction of electroactive chelating groups can significantly improve both the capacity and cycling stability of p-type triphenylamine derivative-based electrodes. The electroactive chelating groups promote a higher proportion of electroactive sites within the cathode material. The combined in/ex situ spectroscopic analysis and theoretical investigations show that electroactive chelating groups facilitate the formation of stable zinc-supramolecular network, which effectively mitigates the dissolution of electrode materials and the decomposition of the aqueous electrolyte during cycling. The as-synthesized poly(1,4-naphthoquinone-1,3,5-tri(4-aminophenyl)benzene) exhibits a high reversible capacity of 311 mAh g<sup>-1</sup> at 50 mA g<sup>-1</sup> and superior rate performance (199 mAh g<sup>-1</sup> at 10 A g<sup>-1</sup>) in aqueous electrolyte. Moreover, it demonstrates excellent stability, retaining 83% to 96% of its capacity over 5000 cycles in various aqueous electrolytes, representing a new record for p-type and bipolar-type organic electrode materials. This work provides valuable insights into the design of organic electrode materials for high-performance ZIBs.

## Introduction

Rechargeable aqueous zinc-ion batteries (ZIBs) represent one of the most promising large-scale energy storage technologies due to their high theoretical capacity (820 mAh g<sup>-1</sup> (Zn metal)), cost-effectiveness, and safety. [1-6] In particular, ZIBs with small organic molecules and polymer-based electrode materials have been extensively studied owing to their sustainability, structural diversity, environmental friendliness, and high theoretical capacity. [7-12] Among various organic

[\*] Dr. J. Zhou+, Dr. P. Guo, J. Jiao, Y. He, Q. Wang, Dr. X. Ding, Dr. D. Liu, Prof. R. Wu

College of Smart Materials and Future Energy, State Key Laboratory of Coatings for Advanced Equipment, Fudan University, Shanghai 200438, China

E-mail: rbwu@fudan.edu.cn

Dr. H. Xu<sup>+</sup>, Prof. J. Li

Department of Materials Science and Engineering, Massachusetts Institute of Technology, Cambridge, MA 02139, USA

E-mail: liju@mit.edu

Prof. J. Li

Department of Nuclear Science and Engineering, Massachusetts Institute of Technology, Cambridge, MA 02139, USA

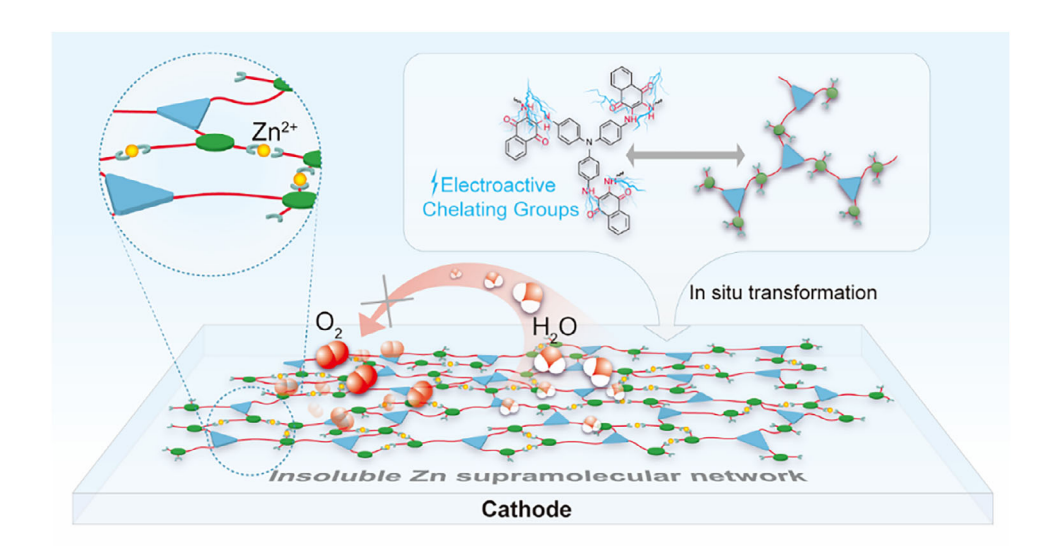
- [+] Both authors contributed equally to this work.
- Additional supporting information can be found online in the Supporting Information section
- © 2025 The Author(s). Angewandte Chemie International Edition published by Wiley-VCH GmbH.. This is an open access article under the terms of the Creative Commons Attribution License, which permits use, distribution and reproduction in any medium, provided the original work is properly cited.

electrode materials (OEMs), p-type OEMs with anion storage mechanisms (e.g., triphenylamine derivatives) can be oxidized to a positively charged state and demonstrate rapid kinetics and relatively high redox potential.[3,13-15] However, the limited capacity and poor stability of p-type OEMs have hindered their commercialization.[13]

The low capacity of p-type OEMs arises from the low proportion of electroactive groups within their overall structure. Taking triphenylamine derivatives as an example, their redox reaction only occurs on the N atom with a singleelectron transfer.[16,17] Therefore, increasing the proportion of electroactive structures within the molecules is an effective strategy to enhance the capacity. For example, Zhang et al. employed -NH- groups to link triphenylamine molecules through polymerization, resulting in a capacity of 210.7 mAh g<sup>-1</sup> at a current density of 500 mA g<sup>-1</sup>.[18] Wang et al. introduced n-type redox groups into p-type backbone, achieving a capacity of 188.2 mAh g<sup>-1</sup> at a current density of 40 mA g<sup>-1</sup>.<sup>[19]</sup> Despite the improved capacity, these electrode materials still suffer from poor cycling stability in aqueous electrolytes. Especially, the capacity of ZIBs using triphenylamine derivatives as the cathode material decays rapidly after only a few hundred cycles.[18,20,21]

The poor cycling stability of p-type OEMs is primarily attributed to the high solubility of intermediates in aqueous electrolytes and the decomposition of the electrolyte, particularly the occurrence of oxygen evolution at high voltages during charging.[13,21,22] To date, designing polymer-based electrodes to stabilize the structure and engineering the electrolyte to inhibit decomposition have been employed to enhance the cycling stability of p-type OEMs.[18,21] However, these approaches either require cumbersome synthesis routes

aded from https://onlinelibrary.wiley.com/doi/10.1002/anie.202513842 by Massachusetts Institute of Technolo, Wiley Online Library on [20/11/2025]. See the Terms and Conditions (https://onlinelibrary.wiley.com/terms-and-conditions) on Wiley Online Library for rules of use; OA articles are governed by the applicable Certains and Conditions (https://onlinelibrary.wiley.com/terms-and-conditions) on Wiley Online Library for rules of use; OA articles are governed by the applicable Certains and Conditions (https://onlinelibrary.wiley.com/terms-and-conditions) on Wiley Online Library for rules of use; OA articles are governed by the applicable Certains and Conditions (https://onlinelibrary.wiley.com/terms-and-conditions) on Wiley Online Library for rules of use; OA articles are governed by the applicable Certains and Conditions (https://onlinelibrary.wiley.com/terms-and-conditions) on Wiley Online Library for rules of use; OA articles are governed by the applicable Certains and Conditions (https://onlinelibrary.wiley.com/terms-and-conditions) on Wiley Online Library for rules of use; OA articles are governed by the applicable Certains and Conditions (https://onlinelibrary.wiley.com/terms-and-conditions) on Wiley Online Library for rules of use; OA articles are governed by the applicable Certains and Conditions (https://onlinelibrary.wiley.com/terms-and-conditions) on Wiley Online Library for rules of use; OA articles are governed by the applicable Certains and the appli



Scheme 1. Schematic representation of the advantages of electroactive chelating groups. The electroactive chelating groups represent those that consist of carbonyl groups and adjacent secondary amine groups. Triangles, circles, and semicircular anchors represent the triphenylamine moieties, the naphthoquinone moieties, and the electroactive chelating groups in PNTB, respectively.

or lead to increased costs and sluggish kinetics, while the stability of p-type OEMs remains unsatisfactory. In contrast, the modulation of coordination bonds to introduce a metal-supramolecular structure has rarely received attention in enhancing the cycling stability of OEMs, even though the coordination bonds (e.g.,  $O^- {\cdot \cdot \cdot} Z n^{2+} {\cdot \cdot \cdot} O^-)$  within metalsupramolecular structures have been shown to facilitate cycling stability by stabilizing the structure of OEMs in electrolytes.[16,23] The underlying reason is that these coordination bonds consist solely of Zn2+...O- interactions, which form exclusively during the discharge process and lack the stability required to sustain the metal-supramolecular structure during charging, as the Zn<sup>2+</sup> cations are extracted from the structure. Consequently, their contribution to stability improvements is severely limited, particularly for p-type OEMs. Strengthening the coordination bonds between Zn<sup>2+</sup> and the electrode materials is anticipated to promote the formation of a stable metal-supramolecular structure across a wide voltage range, thereby improving the long-term performance of p-type OEMs.

In this work, we synthesized a triphenylamine derivative, poly(1,4-naphthoquinone-1,3,5-tri(4-aminophenyl)benzene) (denoted as PNTB), through a condensation reaction between 2,3-dichloro-1,4-naphthoquinone and aminophenyl)amine in a NaCl aqueous solution. The as-synthesized PNTB has abundant electroactive chelating groups consisting of carbonyl and secondary amine groups. These electroactive chelating groups not only increase the proportion of electroactive sites within the PNTB structure but also can coordinate with Zn<sup>2+</sup> ions via a strong chelation effect during both discharge and charge processes, forming robust zinc-supramolecular networks that mitigate PNTB dissolution and electrolyte decomposition, thus simultaneously enhancing the capacity and cycling stability (Scheme 1). Consequently, the PNTB cathode exhibited a high reversible capacity of 311.0 mA h g<sup>-1</sup> at 0.05 A g<sup>-1</sup> and 199.0 mA h g<sup>-1</sup> at 10 A g<sup>-1</sup> as well as outstanding stability

across various types of aqueous electrolytes, maintaining 83% to 96% of its initial capacity over 5000 cycles at a current density of 5 A g<sup>-1</sup>. Our study provides a feasible methodology for engineering the structure of organic electrode materials for aqueous ZIBs with high energy density and stability.

### **Results and Discussion**

## **Materials Characterizations**

The PNTB is synthesized via a condensation reaction between 2,3-dichloro-1,4-naphthoquinone and aminophenyl)amine in a molar ratio of 3:2 at 80 °C in NaCl aqueous solution over a period of 10 h (Figure 1a; detailed procedures are provided in the Methods section).<sup>[24]</sup> Scanning electron microscopy (SEM) of PNTB reveals that it has a hollow sphere with a diameter of approximately 4 µm (Figure 1b). These PNTB microspheres exhibit good crystallinity, as indicated by the X-ray diffraction (XRD) pattern (Figure S1), with a specific surface area of 7.9 m<sup>2</sup> g<sup>-1</sup> (Figure S2). Gel permeation chromatography (GPC) was conducted to determine the molecular weight distribution of PNTB. The number-average molecular weight  $(M_n)$  was found to be 13 426 g mol<sup>-1</sup> (Figure S3). Fourier transform infrared (FTIR) spectroscopy was performed to confirm the chemical structure of the PNTB (Figure 1c). Specifically, the peak at 1676 cm<sup>-1</sup> in PNTB corresponds to the stretching vibrations of the C=O group in the naphthoquinone moiety, which originates from 2,3-dichloro-1,4-naphthoquinone. In addition, upon the reaction, the N-H stretching vibration peaks changed from three distinct peaks (3213 to 3408 cm<sup>-1</sup>) to a single peak (3303 cm<sup>-1</sup>), and the wide peaks corresponding to the wagging vibration of -NH2 groups (589 to 792 cm<sup>-1</sup>) disappeared. These indicate the conversion of -NH<sub>2</sub> groups in tris(4-aminophenyl)amine to -NH- groups in PNTB. Moreover, solid-state <sup>1</sup>H and <sup>13</sup>C NMR spectra of 4000

led from https://onlinelibrary.wiley.com/doi/10.1002/anie.202513842 by Mas

Institute of Technolo, Wiley Online Library on [20/11/2025]. See the Terms and Conditions (https://onlinelibrary.wiley.com/terms-and-conditions) on Wiley Online Library for rules of use; OA articles are governed by the applicable Cerative Commons

Figure 1. Synthesis and characterization of PNTB. a) Schematic illustration of the synthesis of PNTB. Electroactive chelating groups are highlighted in red color. b) SEM image of the PNTB. c) FTIR spectra of PNTB, 2,3-dichloro-1,4-naphthoquinone and tris(4-aminophenyl)amine. X-ray photoelectron spectra of the d) N 1s and e) O 1s region of PNTB.

402 400 398

Binding energy (eV)

410 408

PNTB further verified the structure of PNTB (Figures S4 and S5). The X-ray photoelectron spectroscopy (XPS) analysis further reveals that the N 1s spectrum of PNTB exhibits two peaks at 400.9 and 399.7 eV, corresponding to the NPh<sub>3</sub> and Ar—NH—Ar species in the PNTB backbone (Figure 1d), respectively. Moreover, the O 1s spectrum displays a single peak, which is attributed to the C=O groups (Figure 1e). The results above validate the successful synthesis of the PNTB compound. Thermogravimetric analysis (TGA) of PNTB demonstrates its good thermal stability, with 5% weight loss occurring at temperatures up to 289 °C (Figure S6).

## **Electrochemical Performance**

2500

Wavenumber (cm

2000

To investigate the electrochemical performance of the PNTB cathode in aqueous zinc-ion batteries, PNTB was blended with Ketjen black, polyvinylidene difluoride (PVDF), and N-methylpyrrolidone (NMP) to form a homogeneous slurry. The slurry was then uniformly cast onto carbon cloth to fabricate the cathodes, which were subsequently paired with zinc foil to assemble PNTB//Zn metal coin cells. Various aqueous electrolytes were employed in PNTB//Zn batteries, including 2 M zinc sulfate (ZnSO<sub>4</sub>), 3 M zinc trifluoromethanesulfonate (Zn(OTf)<sub>2</sub>), and 1 M Zn(OTf)<sub>2</sub> in a poly(ethylene glycol) (PEG)/water solution with a 1:1 mass ratio. Among these electrolytes, the 1 M Zn(OTf)<sub>2</sub> in PEG/water electrolyte exhibited the highest specific capacity and was consequently selected for subsequent experiments (Figure S7). Figure 2a shows the cyclic voltammetry (CV) curve of PNTB cathodes,

measured at a scan rate of 1 mV s<sup>-1</sup> over a potential range of 0.1-1.7 V. Four oxidation peaks (0.79, 0.90, 1.27, and 1.43 V) and three reduction peaks (0.64, 1.11, and 1.28 V) appeared in the anodic and cathodic scans, respectively, suggesting that the charge storage of PNTB occurs through a multi-step process. The fewer reduction peaks result from peak overlap caused by the rapid reaction kinetics.<sup>[25]</sup> The charge/discharge profiles of PNTB at various current densities exhibit two distinct plateau potential regions, approximately 1.0-1.2 V and 0.5-0.7 V during discharge, and 0.7-1.0 V and 1.3-1.5 V during charge, respectively, further verifying its multi-step charge storage mechanism (Figure 2b). The PNTB cathode can deliver specific capacities of 311, 288, 276, 254, 241, 230, 224, 215, and  $199 \text{ mAh g}^{-1}$  at current densities of 0.05, 0.1, 0.2, 0.5, 1, 2, 3, 5, and 10 A g<sup>-1</sup>, respectively, demonstrating high specific capacities and excellent rate performance. This favorable rate performance is also observed in the high-mass-loading cell, although with a noticeably lower specific capacity (Figure S8). Note that all the specific capacities are calculated based on the mass loading of active material (PNTB). To exclude the influence of the carbon conductor on the evaluation of PNTB electrode performance, its contribution to the overall capacity was also systematically measured. As illustrated in Figure S9, specific capacities of 32 and 20 mAh g<sup>-1</sup> were observed for the carbon conductor electrode at 0.1 and 5 A  $g^{-1}$ , respectively, indicating a negligible capacity contribution of the carbon conductor in the PNTB cathode. The exceptionally high capacity of PNTB can be ascribed to the introduced electroactive chelating groups (i.e., C=O and -NH-), which enable a high ratio of electroactive groups within the PNTB

534 532

Binding energy (eV)

## Research Article

ded from https://onlinelibrary.wiley.com/doi/10.1002/anie.202513842 by Massachusetts Institute of Technolo, Wiley Online Library on [20/11/2025]. See the Terms and Conditions (https://onlinelibrary.wiley.com/doi/10.1002/anie.202513842 by Massachusetts Institute of Technolo, Wiley Online Library on [20/11/2025]. See the Terms and Conditions (https://onlinelibrary.wiley.com/doi/10.1002/anie.202513842 by Massachusetts Institute of Technolo, Wiley Online Library on [20/11/2025]. See the Terms and Conditions (https://onlinelibrary.wiley.com/doi/10.1002/anie.202513842 by Massachusetts Institute of Technolo, Wiley Online Library on [20/11/2025]. See the Terms and Conditions (https://onlinelibrary.wiley.com/doi/10.1002/anie.202513842 by Massachusetts Institute of Technolo, Wiley Online Library on [20/11/2025]. See the Terms and Conditions (https://onlinelibrary.wiley.com/doi/10.1002/anie.202513842 by Massachusetts Institute of Technolo, Wiley Online Library.wiley.com/doi/10.1002/anie.202513842 by Massachusetts Institute of Technology.wiley.com/doi/10.1002/anie.202513842 by Massachusetts Institute of Technology.wiley.

and-conditions) on Wiley Online Library for rules of use; OA articles are governed by the applicable Creative Commons License

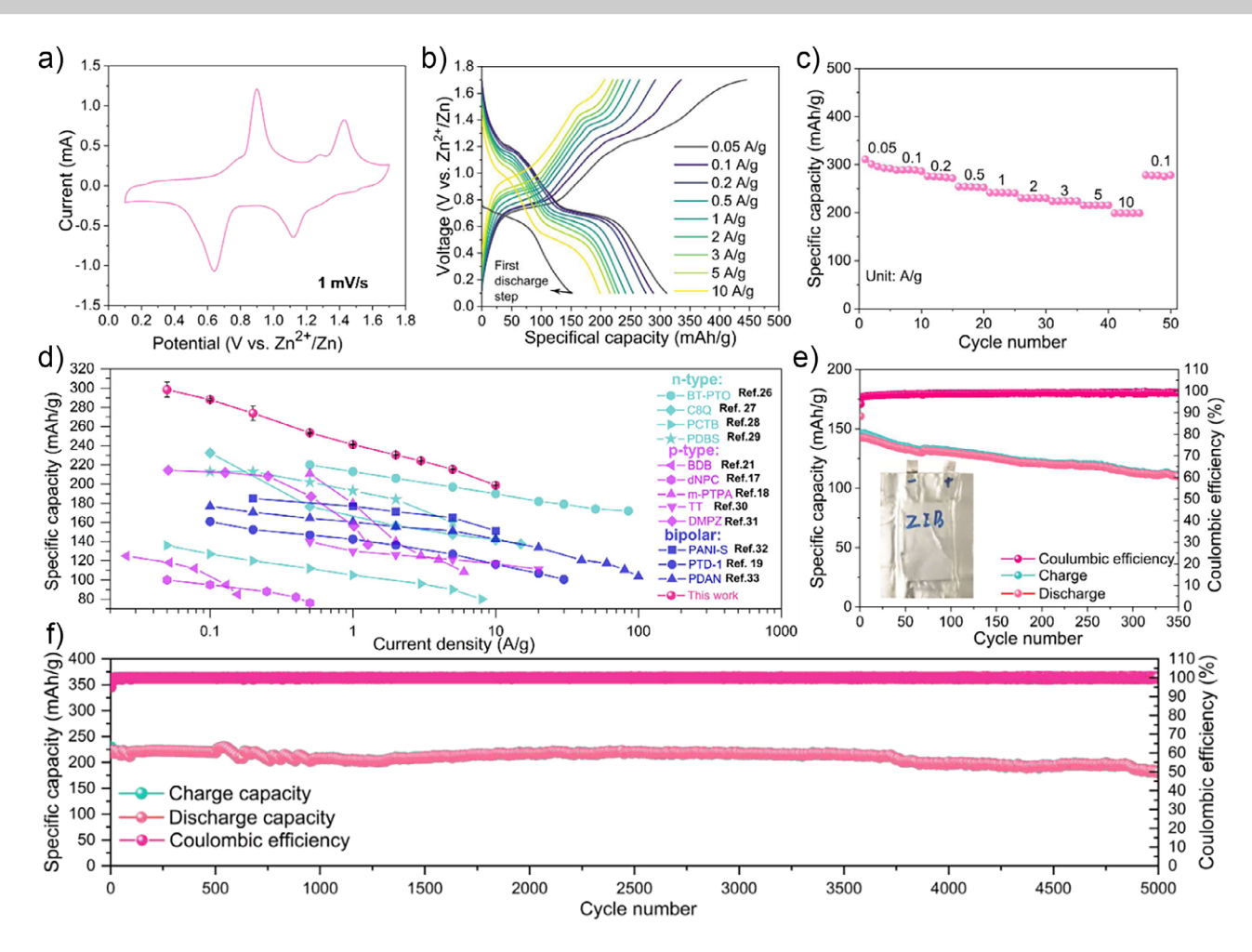


Figure 2. Electrochemical performance of the PNTB cathode. a) Cyclic voltammetry measurement of the PNTB cathode measured at 1 mV s<sup>-1</sup>. b) Charge/discharge curves of PNBT-based ZIB at different current densities. c) Rate performance of PNTB cathode. d) Comparison of the rate performance of the PNTB cathode with other reported organic cathodes for ZIBs. Error bars represent the standard deviation of five replicate measurements in panel (c). Note: Due to differences in testing protocols, this comparison is for general reference only. e) Cycling performance of the PNTB//Zn pouch battery. Inset: photograph of the PNTB//Zn pouch battery. f) Cycling stability of PNTB-cathode measured at a current density of 5 A g<sup>-1</sup>.

backbone, while the good rate performance is attributed to the intrinsically fast reaction kinetics of p-type N-containing moieties within the PNTB structure (Figure 2c). In contrast, one of the reactants of PNTB, i.e., tris(4-aminophenyl)amine, which is p-type and lacks electroactive chelating groups, exhibited a significantly lower capacity that declined sharply within a few cycles (Figure S10). Note that the capacity of PNTB surpasses those of most reported OEMs and is significantly superior to the p-type and bipolar-type OEMs (Figure 2d and Table S1).[13] The Ragone plot (calculated according to Figure 2b) demonstrates a high energy density of 236 Wh kg<sup>-1</sup> (cathode active material, CAM) with a power density of 40 W kg<sup>-1</sup> (CAM). Moreover, a high-power density of 7177 W kg<sup>-1</sup> (CAM) can still be achieved at 138 Wh kg-1 (CAM), which is superior to most reported OEMs (Figure \$11).

To further validate its remarkable electrochemical performance, a PNTB//Zn pouch battery was fabricated by stacking two  $2.5 \times 4 \text{ cm}^2$  PNTB cathodes, two  $2.5 \times 4 \text{ cm}^2$  zinc foils, and three  $3 \times 5.5 \text{ cm}^2$  glass fiber separators. This

pouch PNTB//Zn battery exhibited a specific capacity of 150 mAh g<sup>-1</sup> at a current density of 2 A g<sup>-1</sup> and exhibited stable cycling performance over 350 charge/discharge cycles (Figures 2e and S12). In addition, the pouch battery demonstrates stable performance while powering an electrical clock and remains resistant to mechanical deformation (see Supporting Information Video 1). Furthermore, the cycling stability of the PNTB cathode was investigated at 5 A g<sup>-1</sup> (Figures 2f and S13), demonstrating a cycle life of 5000 cycles with nearly 100% Coulombic efficiencies and a capacity retention of 83% (180 mAh g<sup>-1</sup>). The overall integrity of the cathode shows no significant changes before and after cycling (Figure \$14). It is worth mentioning that PNTB demonstrated even better cycling stability in aqueous ZnSO<sub>4</sub> and Zn(OTf)2 electrolytes, with capacity retention rates of 88% (declining from 176 to 154 mAh  $g^{-1}$ ) and 96% (declining from 162 to 156 mAh g<sup>-1</sup>), respectively, after 5000 cycles at a current density of 5 A g<sup>-1</sup> (Figure S15). Compared to other OEMs, particularly triphenylamine derivative-based cathodes that exhibit a significant capacity degradation within a few

wild be a from the Scientific and the second of the second

,

thousand cycles, PNTB demonstrates remarkably superior cycling stability.<sup>[18,20,21]</sup>

The electrochemical performance of PNTB was subsequently investigated by cyclic voltammetry (CV) at different scan rates. As shown in Figure \$16a, similar shapes with slight polarization are observed for CV plots at scan rates from 0.4 to 5 mV s<sup>-1</sup>. The relation between redox peak current i and the potential sweep rate v follows the power-law equation of  $i = av^b$ , where a and b are the adjustable parameters. Figure \$16b shows that the fitted values of b are close to 1.0, with specific values of 0.93, 0.86, 0.88, and 0.70 for peaks 1, 2, 3, and 4, respectively, suggesting that the redox reactions of the PNTB cathode are primarily governed by a capacitive process. To further study the contribution of the capacitivecontrolled capacity in the total capacity, the current for CV tests is divided into two components ( $i = k_1 v + k_2 v^{1/2}$ ), i.e., capacitive  $(k_1 v)$  and diffusion-controlled  $(k_2 v^{1/2})$  processes. Figures \$16c and 16d suggest that the capacitive contribution to the overall capacity increases from 57% to 86% as the scan rate increases from 0.4 to 5 mV s<sup>-1</sup>. This result confirms that the capacitive process predominates at higher rates, which contributes to improved rate capability.

### Charge-Storage Mechanism of PNTB

To gain a deeper understanding of the excellent performance of the PNTB cathode and the impact of electroactive chelating groups on its performance, the charge storage mechanism was investigated through in situ FTIR measurements at various charge and discharge states. The measurements were conducted in attenuated total reflection (ATR) mode, and the charge/discharge states were recorded using cyclic voltammetry (CV) at a scan rate of 0.8 mV s<sup>-1</sup> (Figure S17). To obtain clear FTIR spectra during the charge-discharge process, the spectrum at the open-circuit state (0.75 V versus Zn<sup>2+</sup>/Zn) was used as the background. As shown in Figures 3a and S18, the peaks at  $1302 \text{ cm}^{-1}$  and  $1598 \text{ to } 1469 \text{ cm}^{-1}$ exhibit reversible changes during the charge-discharge cycle (0.10 to 1.70 V), corresponding to the stretching vibrations of C-O and C=C/C=N<sup>+</sup>, respectively. Specifically, during the fully discharged process (0.75 to 0.10 V), the peak strength of C=O vibration gradually becomes prominent, which can be attributed to the fact that C=O groups within PNTB are reduced, forming C=O<sup>-</sup> groups that coordinate with Zn<sup>2+</sup>. Simultaneously, this group transformation altered the dipole moment of naphthoquinone moieties, resulting in the appearance of the -C=O stretching vibration peak at 1685 cm<sup>-1</sup> (Figure S18). Moreover, the pronounced Zn 2p peak observed in the ex situ XPS spectra of the PNTB electrode at 0.1 V further verified this Zn<sup>2+</sup> coordination. During this process, considering the polyvalent nature of Zn<sup>2+</sup> and the polycarbonyl structure of PNTB, each Zn<sup>2+</sup> will insert between two PNTB chains by coordination, forming a zinc-supramolecular network structure.[23,34-36] However, the peak intensity associated with C-O groups in PNTB does not immediately decrease during the subsequent chargeinduced oxidation process, even though two distinct oxidation peaks at 0.85 and 1.22 V, corresponding to the oxidation

of C-O and NPh<sub>3</sub>, respectively, were observed in the CV curve. Instead, it remained stable until the battery was charged to 1.25 V. In addition, XPS analysis shows a stronger Zn 2p peak at 0.90 V compared to that at 0.10 V (Figure 3b). This indicates that the C-O- groups are oxidized to C-O• radicals instead of C=O (Figure \$19), while Zn<sup>2+</sup> cations are coordinated with these C-O• radicals rather than being extracted during the discharging process. Such a transformation may contribute to enhanced reaction kinetics and thereby improve the rate performance observed in Figure 2c. To clarify this atypical structural evolution, synchrotron Zn K-edge X-ray absorption near-edge structure (XANES) spectra of the electrode collected at 0.1 and 0.9 V were obtained, which exhibit coordination features similar to those of zinc tetraphenylporphyrin (ZnTPP), suggesting that the -NH- groups in PNTB also coordinate with Zn<sup>2+</sup> to form a chelating complex (Figure 3c). Additionally, the peak observed at 9664 eV can be ascribed to the contribution from Zn···O coordination by comparison with zinc acetate. Their Fourier-transformed  $k^3$ -weighted  $\chi(k)$  spectra of the extended X-ray absorption fine structure (EXAFS) revealed a primary peak at approximately 1.53 Å (uncorrected for phase shift), which can be assigned to Zn-N/O coordination (Figure \$20a). Notably, an additional feature appeared in the 2.5-3.5 Å range (uncorrected for phase shift), indicating a second-shell scattering contribution. To gain deeper insight into the local coordination environment of Zn species in the electrodes, wavelet transform (WT) analysis of the Zn Kedge EXAFS spectra was performed (Figure S20b-f). In the k-space domain, the main intensity maxima for the samples appear at significantly lower k-values (5.35 Å<sup>-1</sup> at 0.1 V and 5.00  $\text{Å}^{-1}$  at 0.9 V) compared to those of the ZnTPP reference (5.7 Å<sup>-1</sup>) and zinc acetate (5.75 Å<sup>-1</sup>).<sup>[37]</sup> This downward shift of the WT maxima suggests that the Zn atoms in the sample are not exclusively coordinated to either N or O atoms but are likely involved in a mixed coordination environment with both nitrogen and oxygen donor atoms. In the R-space domain, a pronounced WT intensity feature was observed in the 2.5–3.5 Å region, which is attributed to second-shell scattering paths, possibly arising from Zn···O—C and/or Zn···N-C interactions that occur in an extended chelating or bridging configuration. The emergence of this second-shell signature further supports the formation of a stable supramolecular coordination network, where Zn<sup>2+</sup> is strongly chelated by PNTB through multiple coordination modes. Therefore, the observed unconventional Zn insertion behavior and structural evolution of the C=O groups can be attributed to the strong chelation between PNTB and Zn<sup>2+</sup>, which thus enhances the stability of the zinc-supramolecular network at high voltage. In other words, in contrast to previously reported OEMs whose coordination bonds break immediately during charge-induced oxidation process,[23,34-36] the PNTB-based zinc-supramolecular structure remains stable due to the chelation effect, therefore mitigating the dissolution of PNTB in the electrolyte and leading to a good cycling stability at the higher voltages.[16,23] The increased intensity of the Zn 2p spectra from 0.1 to 0.9 V may be attributed to the co-insertion of H<sup>+</sup> (Figure S21), leading to the formation of C-OH groups during the discharging

# Research Article

led from https://onlinelibrary.wiley.com/doi/10.1002/anie.202513842 by Massachusetts Institute of Technolo, Wiley Online Library on [20/11/2025]. See the Terms and Cond

conditions) on Wiley Online Library for rules of use; OA articles are governed by the applicable Creative Commons

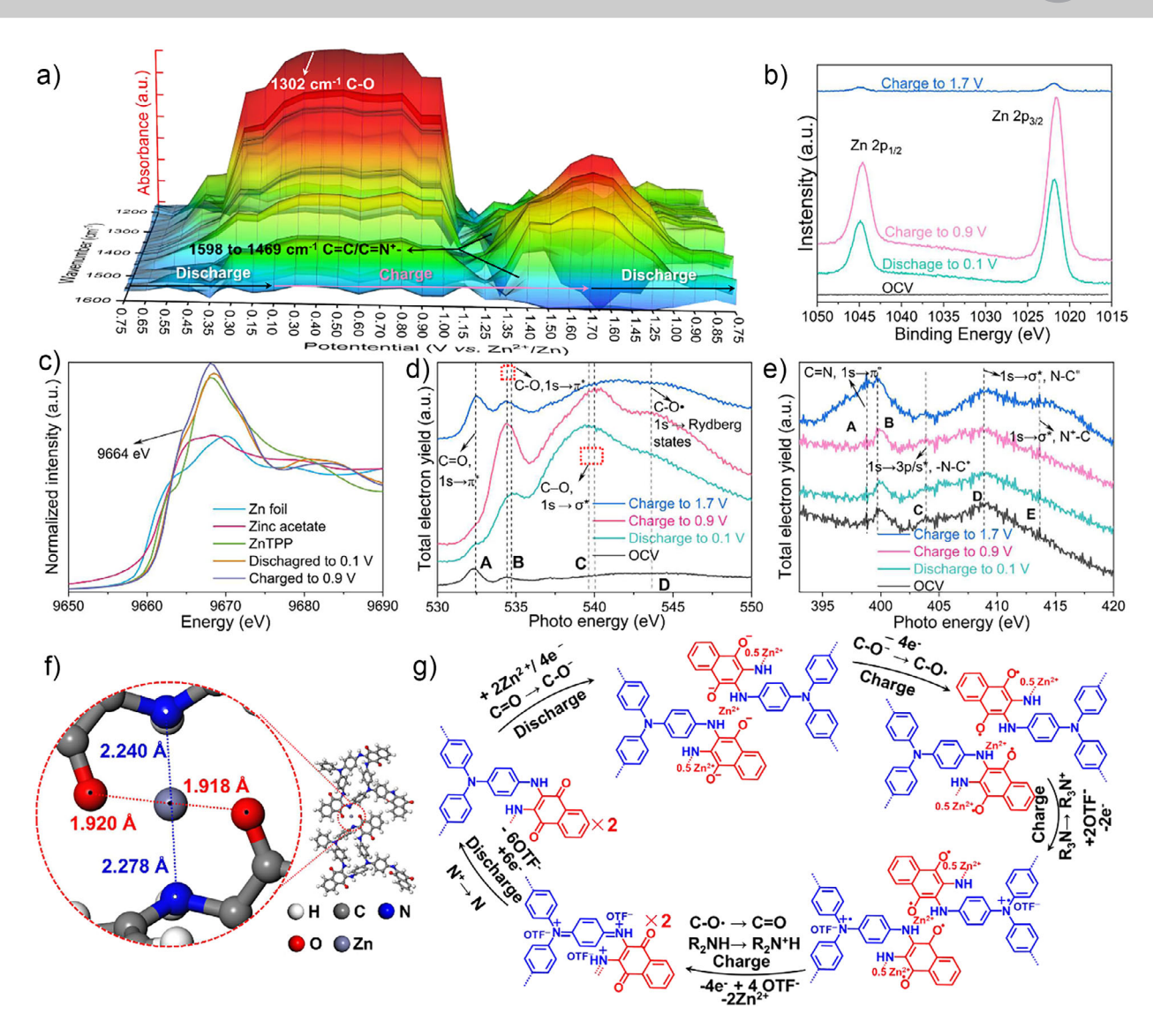


Figure 3. Structural evolution of the PNTB electrode. a) In situ FTIR spectra of PNTB-based cathode at different charge/discharge states with 1 M  $Zn(OTf)_2/(H_2O + PEG)$  electrolyte. b) Ex situ Zn 2p XPS spectra. c) Zn K-edge XANES spectra of the electrode and references. d) O and e) N K-edge XANES of the PNTB-based cathode at the states of open circuit, discharged to 0.1 V, charged to 0.9 V, and charged to 1.7 V. f) The optimized configuration of  $Zn^{2+}$  interacting with PNTB in zinc-supramolecular networks. g) Proposed charge storage mechanism of PNTB cathode, involving the formation of zinc-supramolecular networks.

process.<sup>[26]</sup> Upon subsequent charging process, these C—OH groups could be oxidized to C—O• radicals, which in turn may coordinate with Zn<sup>2+</sup> ions.

As the PNTB cathode continues to be charged (from 1.25 to 1.70 V), the peaks associated with the stretching vibrations of C=C and C=N<sup>+</sup> gradually emerge and intensify, approaching their maximum at 1.70 V. This can be ascribed to the -NH- groups in PNTB being oxidized and the conjugated rearrangement of the C=C bonds in benzene rings. Meanwhile, the peak corresponding to stretching vibrations from C-O disappeared at 1.35 V, and the intensity of the Zn 2p peak in the XPS spectra decreased accordingly at the fully charged state, indicating that the C-O• radicals converted into C=O groups through conjugation-induced bond rearrangement, and Zn<sup>2+</sup> cations were extracted from the zinc-supramolecular networks. This suggests that -NH-

groups in the electroactive chelating groups play a significant role in the formation of the zinc-supramolecular networks, and the oxidation of these -NH- groups leads to the dissociation of these networks. In the second discharge process, the peak intensity from C=C and C=N<sup>+</sup> decreased, suggesting that C=N+ groups are reduced to their initial states. The XPS sulfur (S) 2p spectra at different states further revealed the oxidation of N species (Figure S22), where the peak intensity significantly increased with the insertion of CF<sub>3</sub>SO<sub>3</sub><sup>-</sup> at the fully charged state (1.7 V). The presence of S species was also observed at the state of charging to 0.9 V, which can be ascribed to charge neutralization between CF<sub>3</sub>SO<sub>3</sub><sup>-</sup> and zinc cations in the zinc-supramolecular networks. This is also evident in the shift of the Zn XPS peak toward lower binding energy, from 1044.9 to 1044.6 eV (Figure 3b).

wild be a from the Scientific and the second of the second



The ex situ soft O K-edge X-ray absorption near edge structure (XANES) of the PNTB electrode at different states provides additional insights into the mechanism of charge storage and the formation of the zinc-supramolecular networks (Figure 3c). When discharged to 0.1 V, the intensity of peak A at 532.4 eV corresponding to the 1s $\rightarrow \pi^*$  transition from C=O significantly decreased, while the intensity of peak B at 534.7 eV corresponding to the 1s $\rightarrow \pi^*$  transition from C–O increased. [38] However, the intensity of peak B remains unchanged when charging to 0.9 V, which is consistent with the results observed in the in situ FTIR spectra. Moreover, the peak intensity ratio of B/A increased from 3.8 to 5.9, which may be ascribed to the presence of increased unoccupied states in the C-O• radicals. The peak intensity of peak C, attributed to the 1s $\rightarrow \sigma^*$  transition in the C-O,[38] remained unchanged during the charging process. Furthermore, peak shifts are observed for peak B from 534.7 to 534.3 eV and peak C from 539.6 to 540.0 eV as the charging progresses from 0.10 to 0.90 V. This indicates changes in the chemical state/electronic structure of oxygen atoms, specifically the oxidation process in which C-O groups are converted to C-O• radicals. In addition, peak D at 543.6 eV appears in the spectrum, which can be attributed to the 1s→Rydberg states in C-O• radicals.[39] As the battery was charged to 1.70 V, the intensity of peak B decreased significantly, while the intensity of peak A increased, indicating the conversion of the C-O• radicals into C=O groups. The N K-edge XANES spectra of the PNTB electrode at different states exhibit three characteristic resonances, i.e., 399.6 eV (peak B), 403.8 eV (peak C), and 409.0 eV (peak D) (Figure 3d). Peak B may result from X-ray-induced decomposition, [40] while peaks C and D can be ascribed to the 1 s  $\rightarrow$  sp/s\* and the 1s  $\rightarrow$   $\sigma$ \* transition from N-C, respectively.[40-43] However, when the battery was charged to 1.7 V, new peaks A at 398.7 eV and E at 413.6 eV emerged in the spectrum, which can be attributed to the  $1 \text{ s} \rightarrow \pi^*$  transition in C=N<sup>+</sup> and the  $1 \text{ s} \rightarrow \sigma^*$  transitions in N<sup>+</sup>-C, respectively.<sup>[40]</sup>

DFT calculations were further conducted to investigate the redox chemistry of PNTB and understand the formation of the zinc-supramolecular network. A simplified structure of PNTB, derived from two molecules of tris(4aminophenyl)amine and three molecules of 2,3-dichloro-1,4naphthoquinone, was used to streamline the calculation. The molecular electrostatic potential (ESP) of PNTB showed that regions of negative ESP are predominantly localized on the -C=O groups (blue areas) (Figure \$23), suggesting that these groups function as active sites for Zn<sup>2+</sup> uptake. Correspondingly, the -NH- and NPh3 moieties exhibit positive ESP (red areas), identifying them as the active sites for CF<sub>3</sub>SO<sub>3</sub><sup>-</sup> adsorption. The above results are consistent with the observations from in situ FTIR and ex situ XANES spectra. In addition, the binding energies between PNTB and Zn<sup>2+</sup> in different configurations were calculated. As shown in Figure S24, in comparison with different binding models, Zn<sup>2+</sup> tends to insert between two PNTB chains with the lowest binding energy of -22.7 eV (Figure 3e), suggesting that each -C=O group coordinates 0.5 Zn<sup>2+</sup>. Additionally, upon Zn<sup>2+</sup> insertion, the bond lengths of N-H, C-N, and C-O near the inserted Zn<sup>2+</sup> increase significantly (Table S2), indicating that Zn<sup>2+</sup> adopts tetrahedral coordination through chelation with -NH-C=C-O- moieties (i.e., the electroactive chelating groups) in PNTB. This indicates that the PNTB chains are interconnected through Zn<sup>2+</sup> nodes, establishing a supramolecular network at the fully discharged state, which is similar to that reported for quinone-based electrode materials.[23,34-36] Furthermore, during the subsequent charging process, these supramolecular networks remain stable due to the strong chelation effect. Moreover, the corresponding bond lengths decrease but remain longer than those in the initial state of PNTB (Table S2). As the charging process continues, the N species are oxidized. Considering that PNTB contains secondary nitrogen (-NH-) and tertiary nitrogen (NPh<sub>3</sub>), we calculated the Fukui electrophilic function  $(f^-)$ for the zinc-supramolecular network to determine which N species undergo oxidation first. As shown in Figure \$25, the nitrogen in NPh<sub>3</sub> has a higher  $f^-$ , indicating that it would be oxidized before -NH-, corresponding to the peaks at 1.27 and 1.43 V in the CV curve. This is because NPh<sub>3</sub> has a greater extent of conjugated  $\pi$  bonds compared to -NH-, resulting in a more stable N<sup>+</sup> structure after oxidation.[18]

Accordingly, the PNTB electrode exhibits a bipolar-type charge storage mechanism involving diverse electroactive groups and forming zinc-supramolecular networks during both the discharge and charge processes. The process of structural evolution for the PNTB electrode during the discharging/charging process is illustrated in Figure 3f. When the electrode is fully discharged to 0.1 V, the C=O groups are reduced to C-O<sup>-</sup>, which then chelate with Zn<sup>2+</sup> cations with assistance of -NH- groups, forming zinc-supramolecular networks in which each Zn2+ bridges two PNTB polymeric chains. During the subsequent charging process, the C-Ogroups are oxidized to C-O· radicals, which still chelate with Zn<sup>2+</sup>. As the PNTB electrode is further charged, the zinc-supramolecular network remains stable, while the NPh3 moieties are oxidized to N+Ph3 radical cations, simultaneously binding with OTf<sup>-</sup> anions. As the electrode is further charged to the fully charged state (1.7 V), the -NH- groups are oxidized to be -N+=C cations, resulting in the dissociation of zinc-supramolecular network. Moreover, N+Ph<sub>3</sub> radical cations are also rearranged into N<sup>+</sup> =Ph<sub>3</sub> cations in this process. These  $N^+ = Ph_3$  and  $-N^+ = C$  cations are reduced back to N-Ph<sub>3</sub> and -NH- groups during the subsequent discharge process, restoring the electrode material to its original PNTB structure. This reversible structural evolution also generates strain, which can be visualized by the regular bending and unbending of a free-standing electrode during the charge-discharge process (See Supporting Information

To further demonstrate the significance of the zinc-supramolecular networks on the cycling stability of the cathode, PNTB was carbonylated with ethyl formate (denoted as PNTB-CHO) to reduce the coordination ability of —NH—groups, therefore inhibiting the formation of these networks (Figure 4a). The FTIR spectrum of PNTB-CHO demonstrates a pronounced reduction of -NH- groups (transformed into tertiary amines), as evidenced by the disappearance of the peaks from their characteristic stretching and bending vibration

from https://onlinelibrary.wiley.com/doi/10.1002/anie.202513842 by Mas

Institute of Technolo, Wiley Online Library on [20/11/2025]. See the Terms

itions) on Wiley Online Library for rules of use; OA articles are governed by the applicable Creative Commons

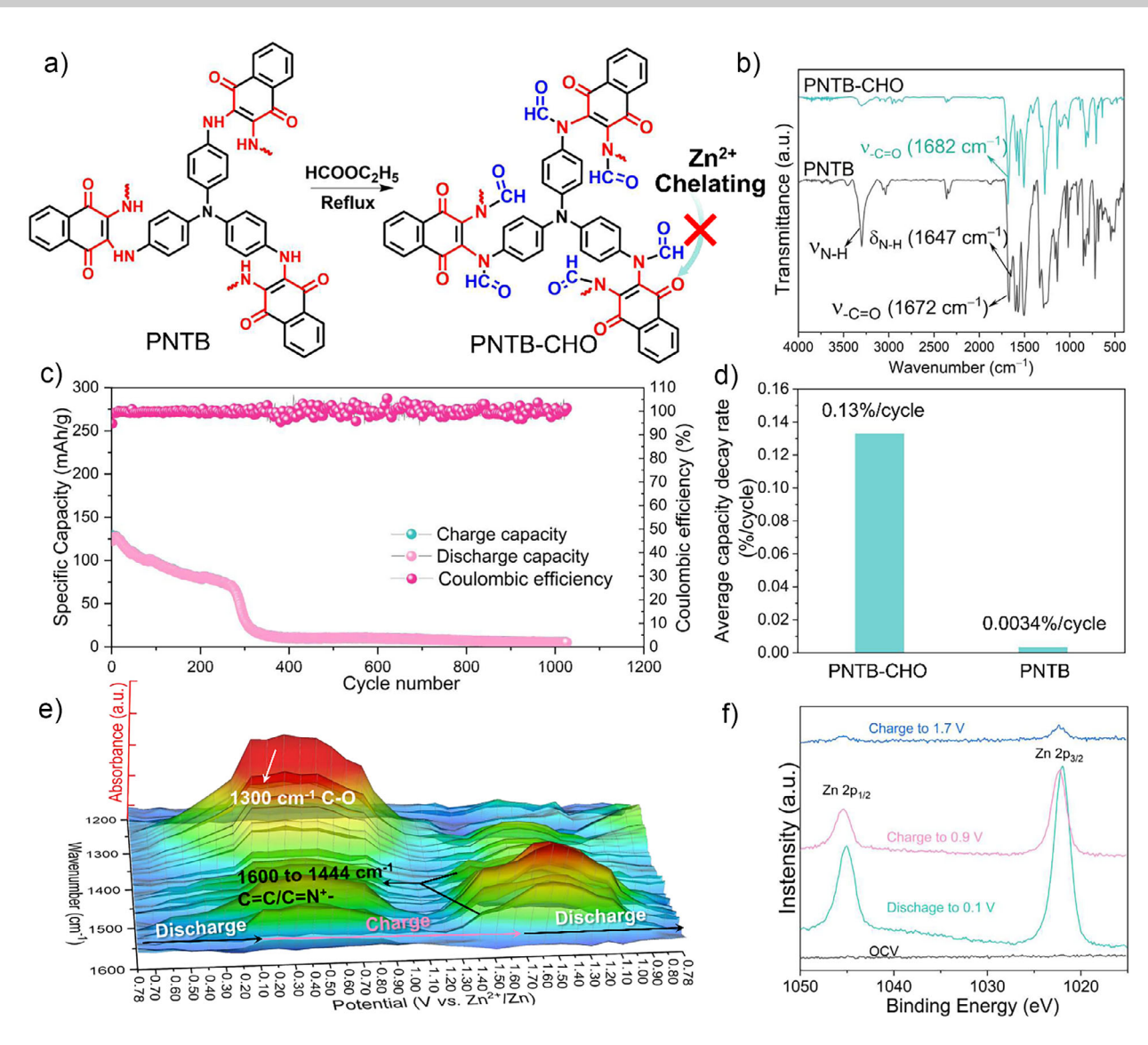


Figure 4. The significance of the zinc-supramolecular networks to the cycling stability. a) Schematic illustration of carbonylated PNTB to inhibit the formation of zinc-supramolecular networks. b) FTIR spectrum of PNTB-CHO in comparison to PNTB. c) Cycling stability of PNTB-CHO-based cathode at 5 A  $g^{-1}$ . d) Comparison of the average capacity decay rate between PNTB and PNTB-CHO. e) In situ FTIR spectra of PNTB-CHO-based cathode at various charge/discharge states. f) The ex situ XPS Zn 2p spectra of PNTB-CHO-based cathode at different charge/discharge states.

(Figure 4b). In parallel, an obvious increase in the intensity of the -C=O stretching vibration is observed compared to that of pristine PNTB, while the rest of the structure remains unchanged. However, the capacity of the PNTB-CHO cathode decreased significantly within merely three cycles, which is markedly inferior to that of PNTB (Figures \$26 and \$27). The capacity of the PNTB-CHO-based cathode showed a rapid decline from 129 to 8 mAh g<sup>-1</sup> after 700 cycles at a current density of 5 A g<sup>-1</sup> (Figure 4c), corresponding to an average capacity decay rate of 0.13% per cycle (Figure 4d). This rate is markedly higher than that of the PNTB cathode, which exhibited a much lower decay rate of 0.0034% per cycle. Similar trends of reduced stability were also observed in the PNTB-CHO//Zn cells with aqueous ZnSO<sub>4</sub> and Zn(OTf)<sub>2</sub> electrolytes (Figure S28). The in situ FTIR analysis revealed that -C=O groups in PNTB-CHO transformed to -C-Ogroups during the initial discharge process. However, unlike in the PNTB cathode, these -C=O groups in PNTB-CHO were immediately oxidized back to -C=O during the subsequent charging process, as evidenced by the decrease in the intensity of the -C-O peak when charged from 0.1 to 1.1 V (Figures 4e and S29). Moreover, in contrast to the intensity increase observed in the PNTB-based electrode (Figure 3b), the ex situ XPS spectra of Zn 2p for PNTB-CHO show a significant decrease in intensity from 0.1 to 0.9 V (Figure 4f), indicating the extraction of Zn<sup>2+</sup>. During this process, a shift peak toward higher binding energy (from 1045.0 to 1045.4 eV) is also observed, suggesting that the coordination bonds between zinc cations and PNTB-CHO are weakened.[26,29] A similar electrode performance was also observed in the cathode based on HCl-treated PNTB (Figures \$30-\$33). The above results suggest that the formation of zincsupramolecular networks is hindered in the PNTB-CHObased cathode, resulting in an inferior cycling stability.

ded from https://onlinelibrary.wiley.com/doi/10.1002/anie.202513842 by Massachusetts Institute of Technolo, Wiley Online Library on [20/11/2025]. See the Terms and Condition

conditions) on Wiley Online Library for rules of use; OA articles are governed by the applicable Creative Commons License

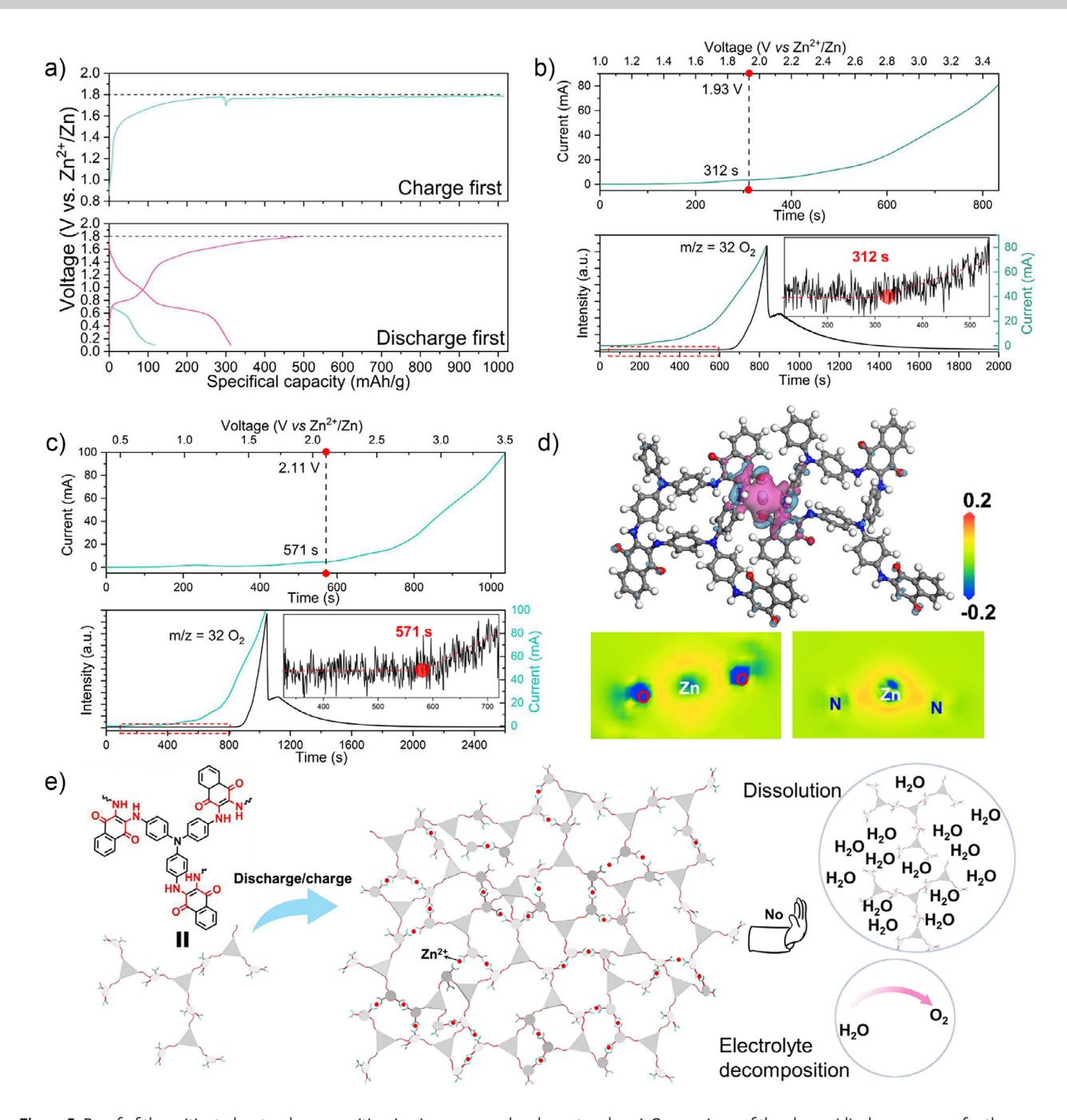


Figure 5. Proof of the mitigated water decomposition in zinc-supramolecular networks. a) Comparison of the charge/discharge curves for the PNTB-based cathode within the voltage range of 0.1 to 1.8 V under conditions of initial charge and initial discharge step. Profiles of oxygen evolution during initial b) charging and c) initial discharging followed by charging from open-circuit voltage to 3.5 V versus  $Zn^{2+}/Zn$ , obtained by LSV and DEMS. The upper panels show the LSV curves along with the corresponding time. The lower panel shows time-resolved LSV curves and the corresponding oxygen evolution profile measured by DEMS. Inset: a partial enlargement of the curve within the red box. d) Electron density difference map for  $Zn^{2+}$  chelating with PNTB. e) Schematic illustration of the formation of zinc-supramolecular networks and their contribution to electrode performance.

Moreover, the charging/discharging curve at a higher potential range (0.1 to 1.8 V) revealed that zinc-supramolecular networks also facilitate mitigating the decomposition of aqueous electrolyte. As demonstrated in Figure 3, the zinc-supramolecular networks form only when PNTB undergoes both discharging and charging processes in sequence, whereas charging from the initial state of PNTB

alone will not form these networks due to the absence of  $Zn^{2+}$ . As shown in Figure 5a, significant electrolyte decomposition occurred in the battery that underwent the initial charging process (top panel), resulting in the charge voltage of the battery being lower than 1.8 V. Similar electrolyte decomposition can also be found in the batteries with  $ZnSO_4$  and  $Zn(OTf)_2$  aqueous electrolyte (Figure S34).

wnloaded from https://onlinelibrary.wiley.com/doi/10.1002/anie.202513842 by Massachusetts Institute of Technolo, Wiley Online Library on [20/11/2025]. See the Terms and Conditions (https://onlinelibrary.wiley.com/

and-conditions) on Wiley Online Library for rules of use; OA articles are governed by the applicable Creative Commons License

## Research Article



In contrast, no such intensive electrolyte decomposition was observed in the battery that underwent the initial discharge process (bottom panel), which formed zinc-supramolecular networks during the discharging and charging process. Moreover, the electrode based on PNTB-CHO still exhibited noticeable electrolyte decomposition at high voltage, despite having undergone the discharge step initially (Figure \$35). This suggests that the presence of zinc-supramolecular networks plays a crucial role in mitigating water oxidation in the electrolytes.<sup>[21]</sup> Differential electrochemical mass spectrometry (DEMS) further confirmed the suppression of the oxygen evolution reaction by zinc-supramolecular networks. During initial charging of the battery from opencircuit voltage (1.00 to 3.5 V versus Zn2+/Zn), oxygen evolution was detected at a potential of 1.93 V versus Zn<sup>2+</sup>/Zn (Figure 5b). However, when the battery underwent an initial discharge step, the oxygen evolution during the subsequent charging process (0.39 to 3.5 V versus Zn<sup>2+</sup>/Zn) occurred at a higher potential of 2.11 V versus Zn<sup>2+</sup>/Zn (Figure 5c). Please note that the potentials mentioned above do not reflect the actual practical oxygen evolution potentials due to time delays during gas transfer from the battery to the mass spectrometer. This may be attributed to the influence of the zinc-supramolecular networks on the formation or effectiveness of the passivation layer, which is considered beneficial for mitigating water decomposition. Moreover, the Zn<sup>2+</sup> nodes within the zinc-supramolecular networks induce electron localization toward Zn<sup>2+</sup> (Figure 5d), therefore may impede electron transfer across the networks. Furthermore, this electron localization may further hinder the adsorption and diffusion of water molecules on the PNTB backbone, particularly on the N+Ph3 radical cations, which are considered the primary active sites responsible for driving water oxidation,[21,45] thereby facilitating the mitigation of water decomposition. Therefore, the electroactive chelating groups in PNTB facilitate the formation of stable zincsupramolecular networks, which play an important role in decreasing the solubility of PNTB in the electrolyte and mitigating electrolyte decomposition, enabling good cycling stability (Figure 5e).

#### Conclusion

In summary, we introduced electroactive chelating groups into a triphenylamine derivative-based cathode material (PNTB), achieving a high specific capacity of 311 mAh g<sup>-1</sup> at 50 mA g<sup>-1</sup> and good stability over 5000 cycles at 5 A g<sup>-1</sup>, with 83% of the capacity remaining in 1 M Zn(OTf)<sub>2</sub> PEG/water electrolyte for aqueous ZIBs. Moreover, better cycling stability was achieved using a 3 M Zn(OTf)<sub>2</sub> aqueous electrolyte, with 96% of the capacity retained under the same conditions. The introduction of electroactive chelating groups not only increases the proportion of electroactive sites in PNTB but also enables PNTB to form stable zinc-supramolecular networks through strong chelation with Zn<sup>2+</sup> in a wide voltage range, thus effectively mitigating the dissolution of PNTB in the aqueous electrolyte and reducing electrolyte decomposition during the charge and discharge

process. In addition, the as-synthesized PNTB exhibited good rate capacity due to its rapid reaction kinetics, achieving a high capacity of 199 mAh  $\rm g^{-1}$  at 10 A  $\rm g^{-1}$ . This work provides a new avenue for designing and exploring organic electrode materials with high energy density and stability for aqueous zinc-ion batteries.

## **Supporting Information**

The authors have cited additional references within the Supporting Information.<sup>[46–52]</sup>

## **Acknowledgements**

The authors acknowledge financial support from the National Natural Science Foundation of China (No. 52225104), "Shuguang Program" supported by the Shanghai Education Development Foundation and Shanghai Municipal Education Commission (No. 20SG03). The authors acknowledge funding from China Postdoctoral Science Foundation (2023M740640) and the Postdoctoral Fellowship Program of CPSF (GZC20230460). The authors also acknowledge the staff members of the BL10B (https://cstr.cn/31131.02.HLS.PES) at NSRL for providing characterizations by Synchrotron Radiation.

## **Conflict of Interests**

The authors declare no conflict of interest.

#### **Data Availability Statement**

The data that support the findings of this study are available from the corresponding author upon reasonable request.

**Keywords:** Electroactive chelating groups · Organic electrode · Zinc-ion batteries · Zinc-supramolecular networks

- [1] B. Tang, L. Shan, S. Liang, J. Zhou, Energy Environ. Sci. 2019, 12, 3288–3304, https://doi.org/10.1039/C9EE02526J.
- [2] N. Zhang, X. Chen, M. Yu, Z. Niu, F. Cheng, J. Chem. Soc. Rev. 2020, 49, 4203–4219.
- [3] H. Cui, L. Ma, Z. Huang, Z. Chen, C. Zhi, SmartMat 2022, 3, 565–581.
- [4] A. Mahmood, Z. Bai, T. Wang, Y. Lei, S. Wang, B. Sun, H. Khan, K. Khan, K. Sun, G. Wang, *Chem. Soc. Rev.* 2025, 54, 2369–2435 https://doi.org/10.1039/D4CS00929K.
- [5] G. Mahendra, R. Roy, A. K. Singh, J. Power Sources 2024, 624, 235515, https://doi.org/10.1016/j.jpowsour.2024.235515.
- [6] R. Roy, G. Mahendra, A. K. Singh, J. Chem. Eng. 2024, 500, 156870, https://doi.org/10.1016/j.cej.2024.156870.
- [7] J. Yang, H. Hua, H. Yang, P. Lai, M. Zhang, Z. Lv, Z. Wen, C. C. Li, J. Zhao, Y. Yang, Adv. Energy Mater. 2023, 13, 2204005, https://doi.org/10.1002/aenm.202204005.

oaded from https://onlinelibrary.wiley.com/doi/10.1002/anie.202513842 by Massachusetts Institute of Technolo, Wiley Online Library on [20/11/2025]. See the Terms and Conditions (https://onlinelibrary.wiley.com/terms

and-conditions) on Wiley Online Library for rules of use; OA articles are governed by the applicable Creative Commons

- [8] Z. Song, L. Miao, H. Duan, Y. Lv, L. Gan, M. Liu, Angew. Chem. Int. Ed. 2024, 136, e202401049.
- [9] Q. Zhang, T. Chen, X. Qian, J. Fu, Adv. Energy Materials 2024, 2403392
- [10] X. Yu, K. Zhou, C. Liu, J. Li, J. Ma, L. Yan, Z. Guo, Y. Wang, Angew. Chem. Int. Ed. 2025, 64, e202501359.
- [11] H. Xu, G. Xu, B. Huang, J. Yan, M. Wang, L. Chen, J. Shi, Angew. Chem. Int. Ed. 2023, 62, e202218603.
- [12] R. Roy, RG, A. Basith, R. Banerjee, A. K. Singh, Energy Storage Mate 2024, 71, 103680, https://doi.org/10.1016/j.ensm. 2024.103680.
- [13] Z. Li, J. Tan, Y. Wang, C. Gao, Y. Wang, M. Ye, J. Shen, Energy Environ. Sci. 2023, 16, 2398-2431, https://doi.org/10. 1039/D3EE00211J.
- [14] H. Wang, Q. Wu, L. Cheng, G. Zhu, Coordin Chem. Rev. 2022, 472, 214772,
- [15] M. Hariram, P. K. Pal, A. S. Chandran, M. R. Nair, M. Kumar, M. K. Ganesha, A. K. Singh, B. Dasgupta, S. Goel, T. Roy, P. W. Menezes, D. Sarkar, Small 2025, 21, 2410408, https://doi.org/10. 1002/smll.202410408.
- [16] H. Peng, Q. Yu, S. Wang, J. Kim, A. E. Rowan, A. K. Nanjundan, Y. Yamauchi, J. Yu, Adv. Sci. 2019, 6, 1900431, https://doi.org/10. 1002/advs.201900431.
- [17] U. Mittal, F. Colasuonno, A. Rawal, M. Lessio, D. Kundu, Energy Stor. Mater. 2022, 46, 129-137.
- [18] H. Zhang, L. Zhong, J. Xie, F. Yang, X. Liu, X. Lu, Adv. Mater. 2021, 33, 2101857, https://doi.org/10.1002/adma.202101857.
- [19] N. Wang, Z. Guo, Z. Ni, J. Xu, X. Qiu, J. Ma, P. Wei, Y. Wang, Angew. Chem. Int. Ed. 2021, 60, 20826-20832, https://doi.org/10. 1002/anie.202106238.
- [20] X. Qiu, J. Xu, K. Zhou, X. Huang, M. Liao, Y. Cao, G. Zhou, P. Wei, Y. Wang, Angew. Chem. Int. Ed. 2023, 62, e202304036, https://doi.org/10.1002/anie.202304036.
- [21] H. Glatz, E. Lizundia, F. Pacifico, D. Kundu, ACS Appl. Energy Mater. 2019, 2, 1288–1294, https://doi.org/10.1021/ acsaem.8b01851.
- [22] J. Xiao, Q. Li, Y. Bi, M. Cai, B. Dunn, T. Glossmann, J. Liu, T. Osaka, R. Sugiura, B. Wu, J. Yang, J.-G. Zhang, M. S. Whittingham, Nat. Energy 2020, 5, 561-568, https://doi.org/10. 1038/s41560-020-0648-z.
- [23] Y. Wang, C. Wang, Z. Ni, Y. Gu, B. Wang, Z. Guo, Z. Wang, D. Bin, J. Ma, Y. Wang, Adv. Mater. 2020, 32, 2000338, https://doi. org/10.1002/adma.202000338.
- [24] V. K. Tandon, H. K. Maurya, Tetrahedron Lett. 2009, 50, 5896-5902, https://doi.org/10.1016/j.tetlet.2009.07.149.
- [25] X. Wang, Y. Liu, Z. Wei, J. Hong, H. Liang, M. Song, Y. Zhou, X. Huang, Adv. Mater. 2022, 34, 2206812, https://doi.org/10.1002/ adma.202206812.
- [26] S. Zheng, D. Shi, D. Yan, Q. Wang, T. Sun, T. Ma, L. Li, D. He, Z. Tao, J. Chen, Angew. Chem. Int. Ed. 2022, 61, e202117511, https://doi.org/10.1002/anie.202117511.
- [27] C. Ding, Y. Wang, C. Li, J. Wang, Q. Zhang, W. Huang, Chem. Sci. 2024, 15, 4952-4959, https://doi.org/10.1039/D4SC00491D.
- [28] Y. Zhang, C. Zhao, Z. Li, Y. Wang, L. Yan, J. Ma, Y. Wang, Energy Stor. Mater. 2022, 52, 386-394.
- [29] T. Sun, Z.-J. Li, Y.-F. Zhi, Y.-J. Huang, H. J. Fan, Q. Zhang, Adv. Funct. Mater. 2021, 31, 2010049, https://doi.org/10.1002/ adfm.202010049.
- [30] H. Cui, T. Wang, Z. Huang, G. Liang, Z. Chen, A. Chen, D. Wang, Q. Yang, H. Hong, J. Fan, C. Zhi, Angew. Chem. Int. Ed. 2022, 61, e202203453, https://doi.org/10.1002/anie.202203453.
- [31] M. H. Lee, G. Kwon, H. Lim, J. Kim, S. J. Kim, S. Lee, H. Kim, D. Eum, J.-H. Song, H. Park, W. M. Seong, Y. Jung, K. Kang, ACS Energy Lett. 2022, 7, 3637-3645, https://doi.org/10. 1021/acsenergylett.2c01535.

- [32] H.-Y. Shi, Y.-J. Ye, K. Liu, Y. Song, X. Sun, Angew. Chem. Int. Ed. 2018, 57, 16359–16363, https://doi.org/10.1002/anie.
- [33] L. Yan, Q. Zhu, Y. Qi, J. Xu, Y. Peng, J. Shu, J. Ma, Y. Wang, Angew. Chem. Int. Ed. 2022, 42, e202211107.
- [34] Z. Guo, Y. Ma, X. Dong, J. Huang, Y. Wang, Y. Xia, Angew. Chem. Int. Ed. 2018, 130, 11911-11915, https://doi.org/10.1002/ ange.201807121.
- [35] F. Ye, Q. Liu, H. Dong, K. Guan, Z. Chen, N. Ju, L. Hu, Angew. Chem. Int. Ed. 2022, 61, e202214244, https://doi.org/10. 1002/anie.202214244.
- [36] M. Yu, N. Chandrasekhar, R. K. M. Raghupathy, K. H. Ly, H. Zhang, E. Dmitrieva, C. Liang, X. Lu, T. D. Kühne, H. Mirhosseini, I. M. Weidinger, X. Feng, J. Am. Chem. Soc. 2020, 142, 19570-19578, https://doi.org/10.1021/jacs.0c07992.
- [37] Z. Xia, H. Zhang, K. Shen, Y. Qu, Z. Jiang, Phys. B 2018, 542, 12-19, https://doi.org/10.1016/j.physb.2018.04.039.
- [38] G.-F. Han, F. Li, W. Zou, M. Karamad, J.-P. Jeon, S.-W. Kim, S.-J. Kim, Y. Bu, Z. Fu, Y. Lu, S. Siahrostami, J.-B. Baek, Nat. Commun. 2020, 11, 2209, https://doi.org/10.1038/s41467-020-15782-z.
- [39] F. Frati, M. O. J. Y. Hunault, F. M. F. de Groot, Chem. Rev. 2020, 120, 4056-4110, https://doi.org/10.1021/acs.chemrev.9b00439.
- [40] P. Leinweber, J. Kruse, F. L. Walley, A. Gillespie, K.-U. Eckhardt, R. I. R. Blyth, T. Regier, J Synchrotron Rad 2007, 14, 500-511, https://doi.org/10.1107/S0909049507042513.
- [41] T. Amano, Y. Muramatsu, N. Sano, J. D. Denlinger, E. M. Gullikson, J. Phys. Chem. C 2012, 116, 6793-6799, https://doi. org/10.1021/jp209650t.
- [42] N. Meng, J. Ren, Y. Liu, Y. Huang, T. Petit, B. Zhang, Energy Environ. Sci. 2018, 11, 566–571, https://doi.org/10.1039/ C7EE03592F.
- [43] H. Yabuta, M. Uesugi, H. Naraoka, M. Ito, A. L. D. Kilcoyne, S. A. Sandford, F. Kitajima, H. Mita, Y. Takano, T. Yada, Y. Karouji, Y. Ishibashi, T. Okada, M. Abe, Earth, Planets Space 2014, 66, 156, https://doi.org/10.1186/s40623-014-0156-0.
- [44] F. Wang, Q. Li, J.-O. Park, S. Zheng, E. Choi, Adv. Funct. Mater. 2021, 31, 2007749, https://doi.org/10.1002/adfm.202007749.
- X. Wang, W. Tang, K. P. Loh, ACS Appl. Energy Mater. 2021, 4, 3612–3621, https://doi.org/10.1021/acsaem.1c00031.
- [46] Y. Zhang, Q. Huang, Z. Song, L. Miao, Y. Lv, L. Gan, M. Liu, Adv. Funct. Mater. 2025. 35, 2416415, https://doi.org/10.1002/ adfm.202416415.
- [47] X. Dan, X. Yin, J. Ba, J. Li, Y. Cheng, F. Duan, Y. Wei, Y. Wang, Nano Lett. 2024, 24, 6881–6888, https://doi.org/10.1021/ acs.nanolett.4c00802.
- [48] B. Delley, J. Chem. Phys. 2000, 113, 7756-7764, https://doi.org/ 10.1063/1.1316015.
- [49] S. Grimme, J. of Comput. Chem. 2006, 27, 1787–1799, https://doi. org/10.1002/jcc.20495.
- [50] S. Li, J. Shang, M. Li, M. Xu, F. Zeng, H. Yin, Y. Tang, C. Han, H.-M. Cheng, Adv. Mater. 2023, 35, 2207115, https://doi.org/10. 1002/adma.202207115.
- [51] C. Hu, X. Yang, P. Liu, Z. Song, Y. Lv, L. Miao, M. Liu, L. Gan, J. Mater. Chemi. A 2024, 12, 11867-11874, https://doi.org/10.1039/ D4TA00476K.
- [52] L.-W. Luo, S. Li, M. Li, J. Li, S. shang, C. Han, Energy Stor. Mater. 2025, 81, 104489.

Manuscript received: June 24, 2025 Revised manuscript received: October 05, 2025 Manuscript accepted: October 20, 2025 Version of record online: ■■,